

Electronic supplementary information for

**Visualizing {110} surface structure of equilibrium-form ZIF-8
crystals by low-dose Cs-corrected TEM**

Xiaocang Han,^{a,#} Wenqian Chen,^{b,c,#} Rui Su,^{d,e,#} Yuan Tian,^g Pan Liu,^{a,b,*}, Pengfei Guan,^{e,*} Min
Luo,^b Jiuhui Han,^b Xiaoxiao Cao,^f Ming Pan,^f Mingwei Chen^{g,*}

*Address correspondence to: mwchen@jhu.edu

#These authors contribute equally to this work

This PDF file includes:

Experimental section

Supplementary Figures: Figure S1-S9

Experimental section

Synthesis of Rhombic Dodecahedral ZIF-8 Nanocrystals. Nanocrystalline ZIF-8 was synthesized by a solvothermal method at room temperature.¹ A solution of $\text{Zn}(\text{NO}_3)_2 \cdot 6\text{H}_2\text{O}$ (0.369 g, 1.24 mmol) in 25 mL of methanol (MeOH) is rapidly poured into a solution of 2-methylimidazole (Hmim) precursors (0.821 g, 10 mmol) in 25 mL of methanol under stirring for one hour. The molar ratio of Zn^{2+} : Hmim: MeOH was approximately 1:8:1000. The as-synthesized ZIF-8 crystals were separated from the milky dispersion by centrifugation and following by repeated washing with fresh methanol for three times. Then, the white samples were dried at room temperature under reduced pressure by mechanical pumping. The rhombic dodecahedral ZIF-8 nanocrystals were dispersed in methanol by sonication about 3~5 minutes. After standing still for 3 minutes, the supernatant liquid was dropped onto ultrathin Si_3N_4 membrane (~5 nm) with a silicon-based grid for TEM characterization.

Structure Characterization. All HRTEM images were captured by using JEM ARM-200F electron microscope equipped with a spherical aberration corrector (CEOS GmbH) for the image-forming (objective) lens system at 200kV. A direct-detection electron-counting camera (Gatan K2 summit) was employed for the low-dose Cs-corrected HETRM observations in electron-counting mode with Dose-fractionation function. Before acquiring the HETRM images, the lens aberrations were tuned with less residual spherical aberration remaining (Cs~1 μm). During the TEM image acquisition, we viewed the specimen in diffraction mode to avoid structural damage during sample searching and present enough contrast at a dose rate lower than $\sim 1 \text{ e}/\text{\AA}^2/\text{s}$. The HRTEM images were acquired as a collection of frames at a high frame rate instead of a single image with long exposure, which is able to minimize the influence of sample drift on spatial resolution after sample motion correction of subframes.

HRTEM Image Processing and Simulation. In this work, a modified low-dose image alignment method was used for refined correction of drift and combined with the commercial image alignment method supported by Digital Micrograph software. In brief, a single frame was overlapped several times to increase the contrast of image by the way of multiple periodic translation, which means translation once, overlapping once. The superimposed images are capable of doing drift correction with an appropriate signal to noise ratio. This method is suitable for images with sample drift smaller than one lattice period. For the images with a larger sample drift (>one lattice period), they were first corrected by the commercial Digital Micrograph software package before using the modified low-dose image alignment method. The drift-corrected HRTEM images were denoised by Wiener and motif additions which are commonly used in HRTEM to enhance signal-to-noise ratio for extracting crystallographic information from the images. Both filters were applied to each image to avoid potential artifacts introduced by a

specific filter. The HRTEM images were simulated by using the commercial *QSTEM* software.² Appropriate imaging parameters and aberration coefficients according to experimental conditions were selected for HRTEM images simulation after setting up the ZIF-8 structure model. Specifically, an accelerating voltage of 200 kV was used, with a spherical aberration of $\sim 1\mu\text{m}$, focal spread of 3 nm, and pixel size of 1.3 Å.

Specifically, Wiener filter was commonly applied to improve the visibility of crystalline components in HRTEM images by subtracting the amorphous background signal contributions, based on the work of R. Kilaas,³ used in DigitalMicrograph software. Normally, the filtering of HRTEM images is in frequency space with the background estimated as a radial average of the Fourier transform of the whole image. After the background has been estimated, the computer automatically constructs the filter. Recently, to improve image display and handling, the Butterworth Filter (described in 1930 by the British engineer and physicist Stephen Butterworth) was first used in FFTs to remove high frequency noise and the influence of image edge effects. The gain of an n-order Butterworth low-pass filter is given in terms of the transfer function $H(\omega)$ as:

$$|H(\omega)|^2 = \frac{1}{1 + \left(\frac{\omega}{\omega_c}\right)^{2n}}$$

n: order of filter; ω_c : cutoff frequency. In HRTEM filters, BW n is the order of the Butterworth filter (values: 1-20). A value of 1 produces a gently inclined slope to the filter (gradual cutoff); a value of 3 a more gaussian slope; higher values produce sharper cut offs. BW Ro is the radius (relative distance from the center of the FFT to the edge) at which the filter function drops to half (values: 0.01-3). Using small values will move the cutoff inwards in the FFT removing more of the lower frequency component, and producing a more heavily filtered image - too low a value and you lose your crystalline intensity. For comparison, the filtered HRTEM images with different parameters were shown in **Figure S6**.

Theoretical calculations of ZIF-8 surface energy. In this work, the {110} surface energies of ZIF-8 crystals with different terminations were calculated by **Equation 1**, which considers the ligand molecules at their gaseous states. Since the ligand molecules are coming from the solutions in real experiments, we also calculate the “solvation-corrected” surface energies by **Equation 2**. The structure relaxation was performed with a force tolerance of 0.04 eV/Å. The slab models were built with 5 or 3 layers of ZIF-8 cages for zigzag, armchair and armchair-like surfaces.

Due to a large number of atoms in the ZIF-8 surface cell, the surface energies of modified ZIF-8 surfaces were calculated by a semi-empirical approach within the self-charge-consistent density functional tight-

binding (SCC-DFTB) framework as implemented in the DFTB+ code. The optimized cell parameter was determined to be 17.035 Å, and this relaxed cell was used to generate {110} surface models. As the DFTB method uses orbital overlap integrals and repulse potentials parameterized from the DFT data, the description of structure and energetic properties would suffer from the approximating models and DFT dataset used for parameterization. Currently, there are two sets of DFTB parameterizations for the Zinc-organic systems: the Zinc-organic (“Znorg”) parameter set⁴ that was fitted against Zinc contained bulk compounds; and for Zn-organic complexes, the third-order parametrization for organic and biological systems (“3ob”) parameter set⁵ was fitted using the third order density functional tight binding (DFTB3) model. The “3ob” parameterization has been shown to reduce the over-binding errors of organic molecules in the previous “Znorg” parameter set and improve the description of hydrogen bonds.⁵ In this work, we choose to use the “3ob” parameterization as it provides better description of lattice constants and surface energies in comparison with the “Znorg” parameterization (see **Table 1**). Additionally, the non-bonding van der Waals interactions were described by the DFT-D3 method⁶ with the Beck-Johnson damping.⁷ The solvation free energies of ligand molecules were calculated using DFT. The COnductor-like Screening MOdel (COSMO)⁸ was used to describe the solvation effect. The Perdew-Burke-Ernzerhof (PBE)⁹ exchange correlation functional was employed to describe the exchange-correlation energy. The polarized triple-zeta valence basis set (def2-TZVP)¹⁰ was used to expand the electron wave functions. All DFT calculations were performed by the ORCA quantum chemistry package.^{11,12}

Supplementary Figures

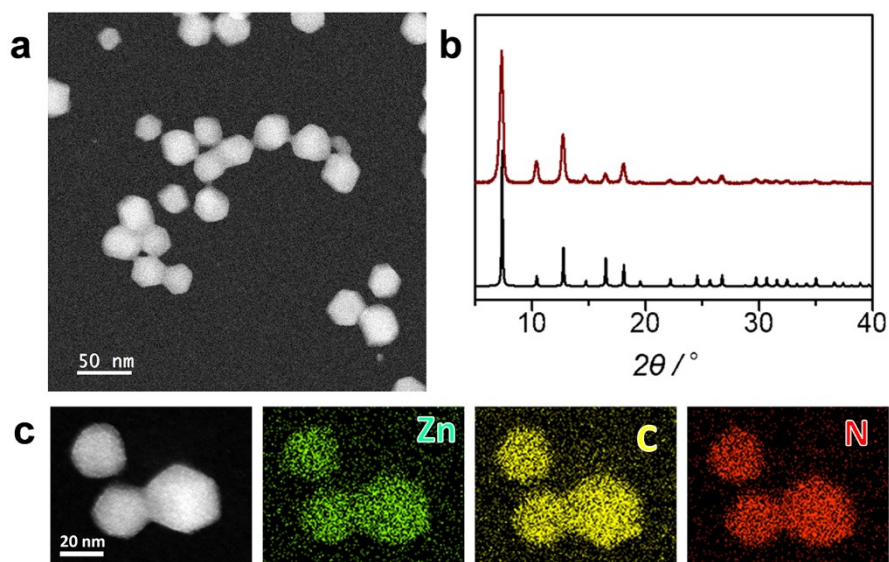


Figure S1. a) STEM image of ZIF-8 crystals. b) Powder X-ray diffraction patterns of the as-synthesized ZIF-8 (red) and simulation (black) from the crystal structure of ZIF-8. c) STEM-EDS chemical mappings of ZIF-8 crystals.

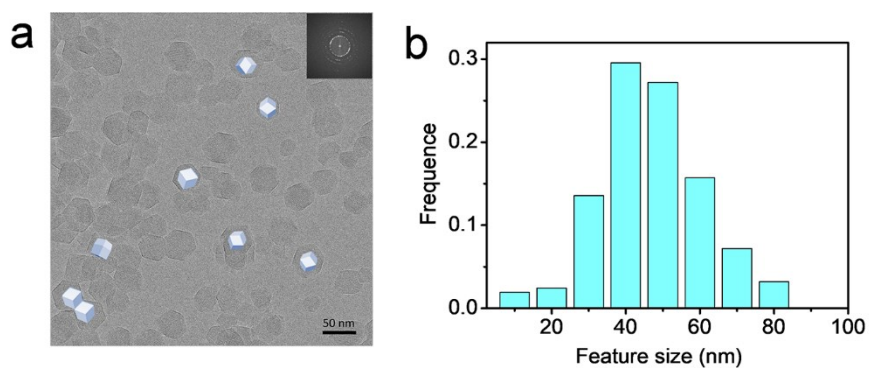


Figure S2. Morphology and particle size distribution of ZIF-8 crystals. a) Low magnification TEM image displays single crystal and agglomerated nanoparticles. The insertions show the projected rhombic dodecahedra models with the same orientation of underneath imaged crystallites. b) Statistical charter of ZIF-8 nanocrystals with a size range between 30-60 nm.

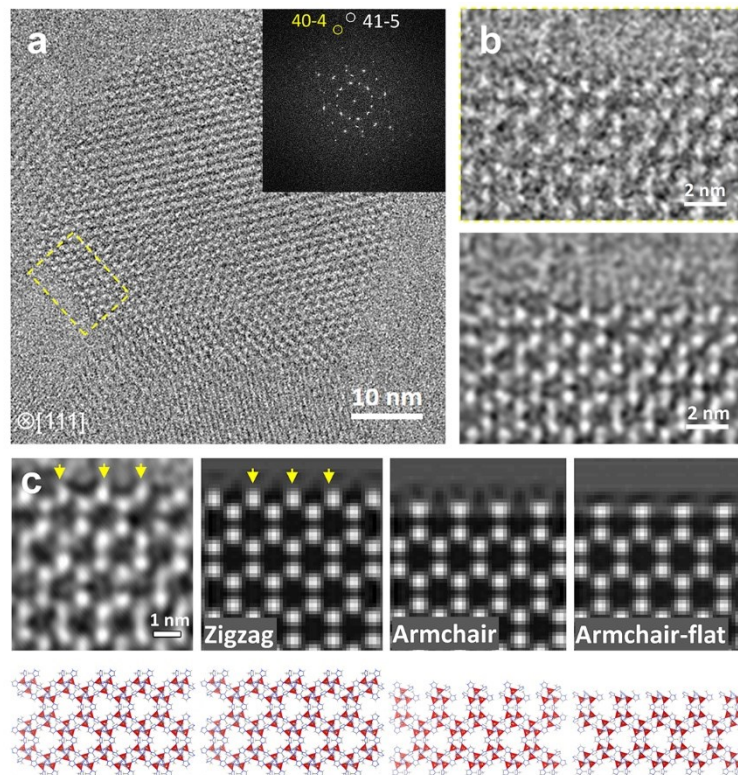


Figure S3. Zigzag surface termination of a ZIF-8 nanocrystal. **a)** The original TEM image taken along $[111]$ direction. Inset: corresponding FFT pattern. **b)** Raw and Wiener filtered HRTEM images (from top to bottom) within region of yellow dashed box in **(a)**, the raw data for **Figure 2c**. The bright spots correspond to Zn triplets. **c)** The comparison of simulated images based on low-panel surface termination models with Wiener filtered experimental image along $[111]$ direction at an overfocus value of 90nm. Clearly, the Wiener filter effectively enhanced the image contrast without introducing artefacts.

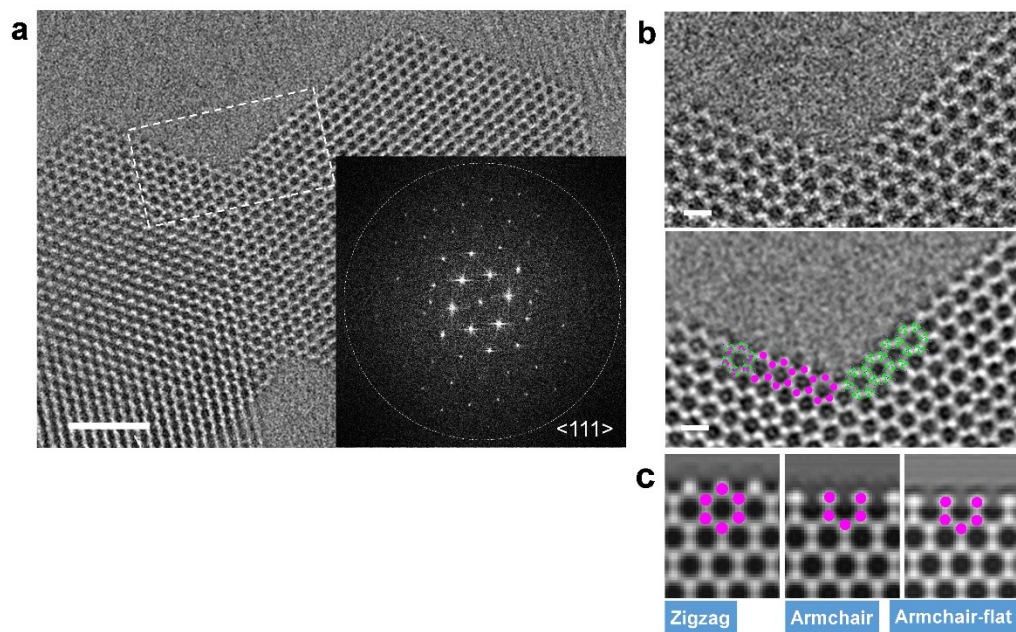


Figure S4. Zigzag surface termination of ZIF-8 nanocrystals. **a)** The original TEM image taken along $[111]$ direction. Inset: corresponding FFT pattern. **b)** Raw and Wiener filtered HRTEM images (from top to bottom) within region of white dashed box in **(a)**. The bright spots correspond to Zn triplets. **c)** The comparison of simulated images based on three surface termination models along $[111]$ direction at an overfocus value of 155nm. Clearly, the Wiener filter effectively enhanced the image contrast without introducing artefacts. Scar bars in **(a, b)**: 10, 2nm.

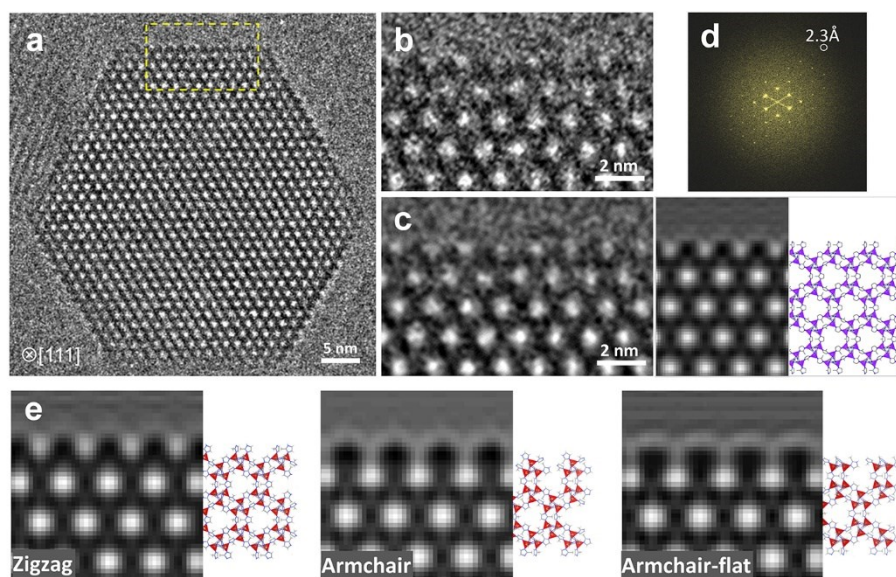


Figure S5. Zigzag surface termination of a ZIF-8 nanocrystal. **a)** The original TEM image taken along [111] direction, the corresponding FFT pattern shown in **(d)**. **b)** Zoom-in HRTEM image of yellow dashed box in **(a)**. **c) Left**, Wiener filtered image of **(b)**; **Middle and right**, simulated (at the defocus value of 220nm) and projected structural model images of ZIF-8 {110} surfaces. The zigzag configuration formed by the close cages is consistent well with the simulated image. **d)** FFT pattern. **e)** The comparison of simulated images based on right surface models along [111] direction. The bright spots correspond to cages positions, where the contrast inversion between **Figure S3** and **S4** is caused by the different defocus values. Consequently, the ZIF-8 {110} surface show a zigzag termination from [111] orientation.

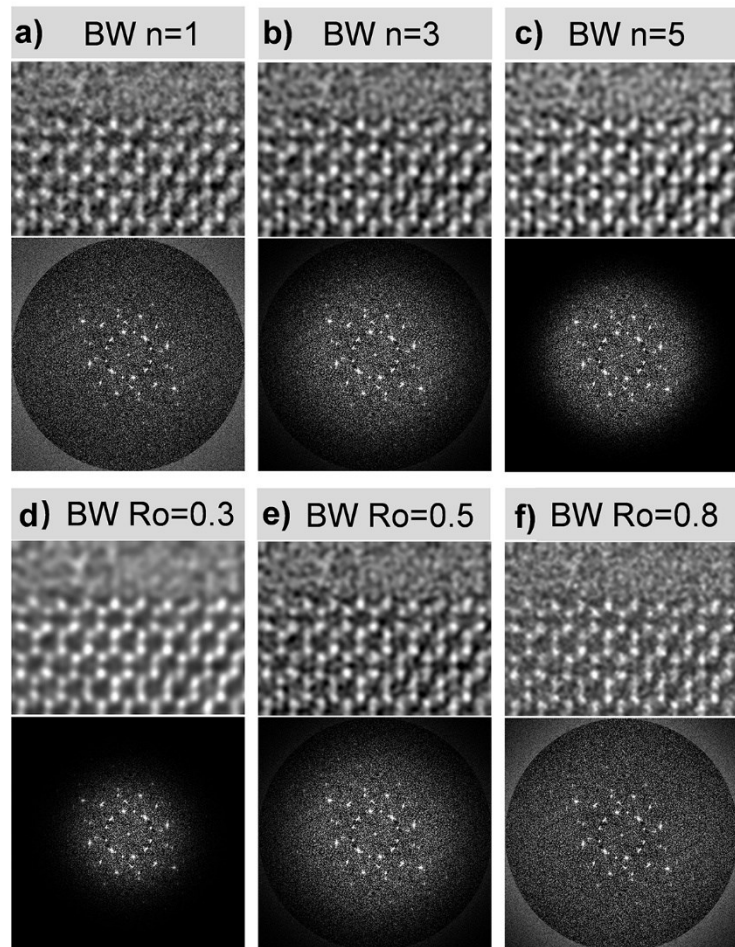


Figure S6. Denoised HRTEM images of ZIF-8 surface with different filter parameters. **a-c)** BW $P_o=0.5$; **d-f)** BW $n=3$. The parameters used in the main text **Fig. 2b-c.** was BW $n=3$, BW $R_o=0.5$. “BW n ” and “BW R_o ” to define the slope of the filter and the radius of the cutoff respectively.

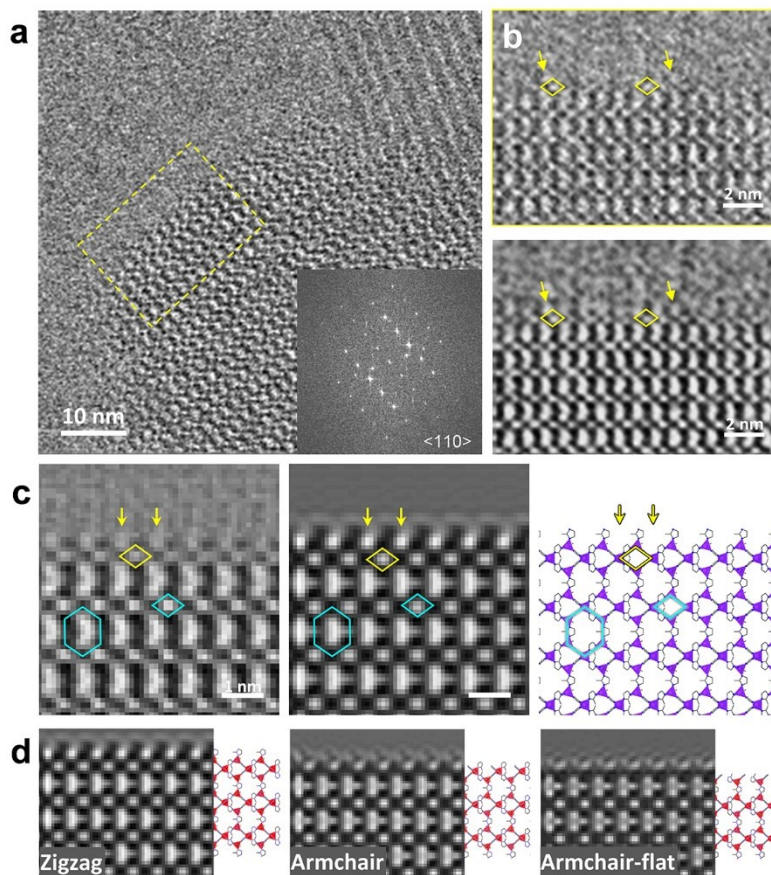


Figure S7. Zigzag surface termination of a ZIF-8 nanocrystal. **a)** The original TEM image taken along $\langle 110 \rangle$ direction. Inset: corresponding FFT pattern. **b)** Raw and Wiener filtered HRTEM images (from top to bottom) within region of yellow dashed box in **(a)**. **c) Left**, real-space superimposing filtered image (over 6 image motifs) in **(b)**; **Middle and right**, simulated (at the defocus value of 68nm) and projected structural model images of ZIF-8 $\{110\}$ surfaces. Along $[011]$ direction, ZIF-8 displays two distinct pore cavities: four-ring and six-ring windows as indicated by rhombus and hexagon frames in both image and structure model. The zigzag configuration formed by the termination of complete four-ring windows (marked by yellow rhombus frame) is consistent well with the simulated image. **d)** The comparison of simulated images based on right surface models along $[011]$ direction. Consequently, the ZIF-8 $\{110\}$ surface show a zigzag termination from $[011]$ crystallographic orientation.

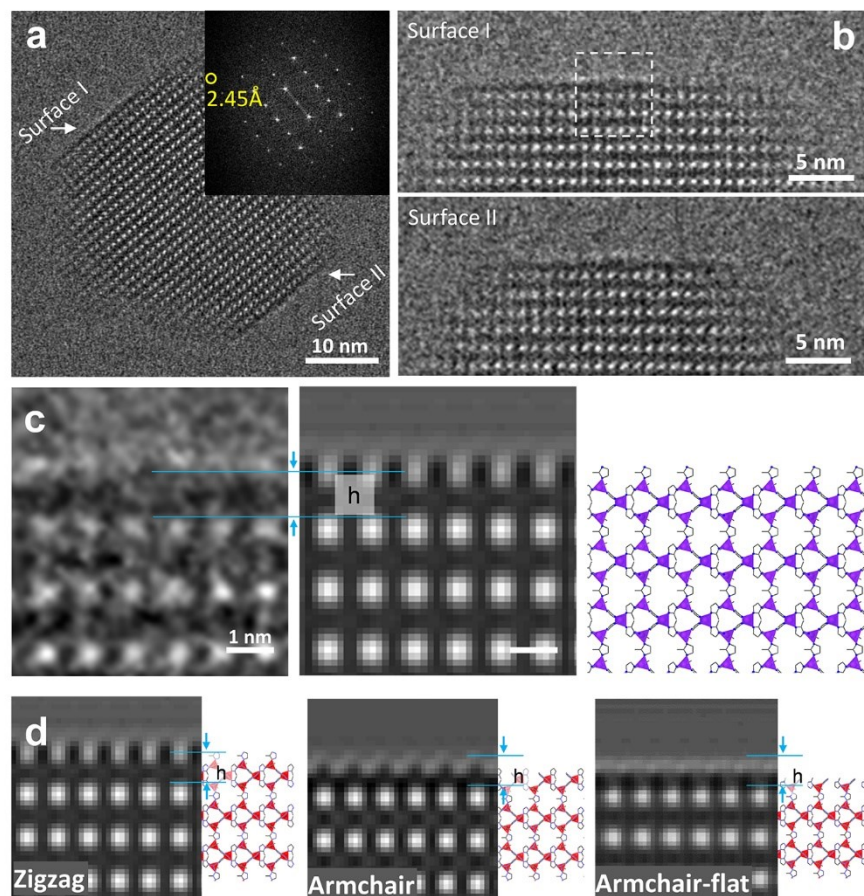


Figure S8. Zigzag surface termination of a ZIF-8 nanocrystal. **a)** The original TEM image taken along $\langle 110 \rangle$ direction. Inset: corresponding FFT pattern. **b)** Zoom-in HRTEM images of two $\{110\}$ surfaces in **(a)**. **c)** **Left**, zoom-in HRTEM image cropped from Surface I; **Middle** and **right**, simulated (at the defocus value of 110nm) and projected structural model images of ZIF-8 $\{110\}$ surfaces. **d)** The comparison of simulated images based on right surface models along $[011]$ direction.

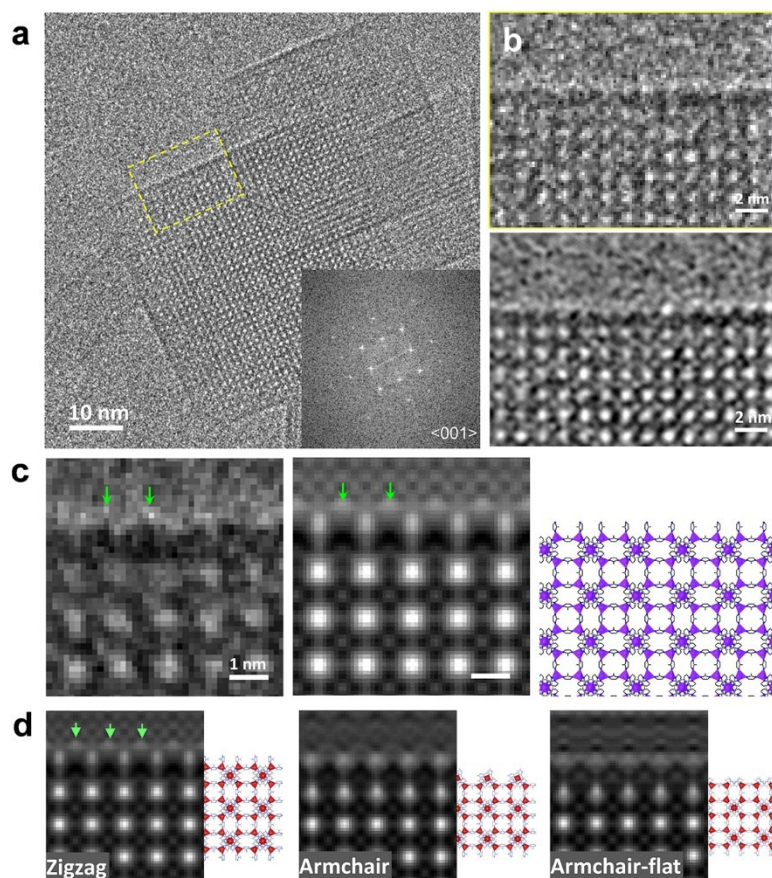


Figure S9. Zigzag surface termination of a ZIF-8 nanocrystal. **a)** The original TEM image taken along $\langle 001 \rangle$ direction. Inset: corresponding FFT pattern. **b)** Raw and Wiener filtered HRTEM images (from top to bottom) within region of yellow dashed box in **(a)**. **c) Left**, real-space superimposing filtered image (over 4 image motifs) in **(b)**; **Middle** and **right**, simulated (at the defocus value of 345nm) and projected structural model images of ZIF-8 $\{110\}$ surfaces. The green arrows highlight the similar contrast between experimental and simulated images on the topmost $\{011\}$ surface. **d)** The comparison of simulated images based on right surface models along $[001]$ direction. Consequently, the ZIF-8 $\{110\}$ surface show a zigzag termination from $[001]$ crystallographic orientation.

References

- 1 J. Cravillon, S. Münzer, S. J. Lohmeier, A. Feldhoff, K. Huber and M. Wiebcke, *Chem. Mater.*, 2009, **21**, 1410–1412.
- 2 C. Koch, *Dissertation*.
- 3 R. Kilaas, *J. Microsc.*, 1998, **190**, 45–51.
- 4 N. H. Moreira, G. Dolgonos, B. Aradi, A. L. Da Rosa and T. Frauenheim, *J. Chem. Theory Comput.*, 2009, **5**, 605–614.
- 5 X. Lu, M. Gaus, M. Elstner and Q. Cui, *J. Phys. Chem. B*, 2015, **119**, 1062–1082.
- 6 S. Grimme, J. Antony, S. Ehrlich and H. Krieg, *J. Chem. Phys.*, 2010, **132**, 154104.
- 7 S. Grimme, S. Ehrlich and LARS GOERIGK, *J. Comput. Chem.*, 2011, **32**, 1456–1465.
- 8 A. Klamt, *J. Phys. Chem.*, 1995, **99**, 2224–2235.
- 9 J. P. Perdew, K. Burke and M. Ernzerhof, *Phys. Rev. Lett.*, 1996, **77**, 3865–3868.
- 10 F. Weigend, M. Häser, H. Patzelt and R. Ahlrichs, *Chem. Phys. Lett.*, 1998, **294**, 143–152.
- 11 F. Neese, *Wiley Interdiscip. Rev. Comput. Mol. Sci.*, 2012, **2**, 73–78.
- 12 F. Neese, *Wiley Interdiscip. Rev. Comput. Mol. Sci.*, 2018, **8**, 4–9.